nature climate change

Supplementary information

https://doi.org/10.1038/s41558-025-02325-x

High-income groups disproportionately contribute to climate extremes worldwide

In the format provided by the authors and unedited

Supplement for Publication ”High-Income Groups Disproportionately Contribute to Climate Extremes Worldwide”

1 INEQUALITY IN CARBON EMISSIONS

We re-processed data on emission and income inequality from ref.[1,2] that is relevant for interpreting our analysis. Emissions in Table S2 are given as CO_2-e emissions and were aggregated using Global Warming Potential (GWP) 100. GWP measures how much energy the emission of a GHG will absorb in the atmosphere over a given period of time (here: 100 years), relative to the emission of the same amount of CO_2.

Accounting from 1990, the top emitters primarily come from the world’s highest emitting countries: the US, China, India and the EU27 (Fig. S1 Panel a&b). Shares of the wealthy have been shifting over the past 30 years: while more than 27% of the global top 10% were European in 1990, this number has dropped to 19% in 2019; and while less than 1% of the global top 10% came from China in 1990, the share has grown to 13% in 2019. While our focus is on wealthy individuals from the world’s largest economies, we note that those from smaller countries also contribute disproportionately, with within country inequalities being even more pronounced in countries in Sub-Saharan Africa and the Middle East and North Africa (MENA) region[1].

We also assess contributions of emitters from selected regions (US, EU27, China, India). Income levels from regional top emitters deviate from their global counter parts, i.e. the top 10%/1% in the US and the EU27 (India and China) are wealthier (poorer) than the globally wealthiest 10%/1% (Fig. S1 Panel c&d, Table S2). In the US, the regional top 10%/1% belong to the globally wealthiest 1-2%/0.1-0.2%. In China, the top 10% were among the globally wealthiest 37% (13%) in 1990 (2019).

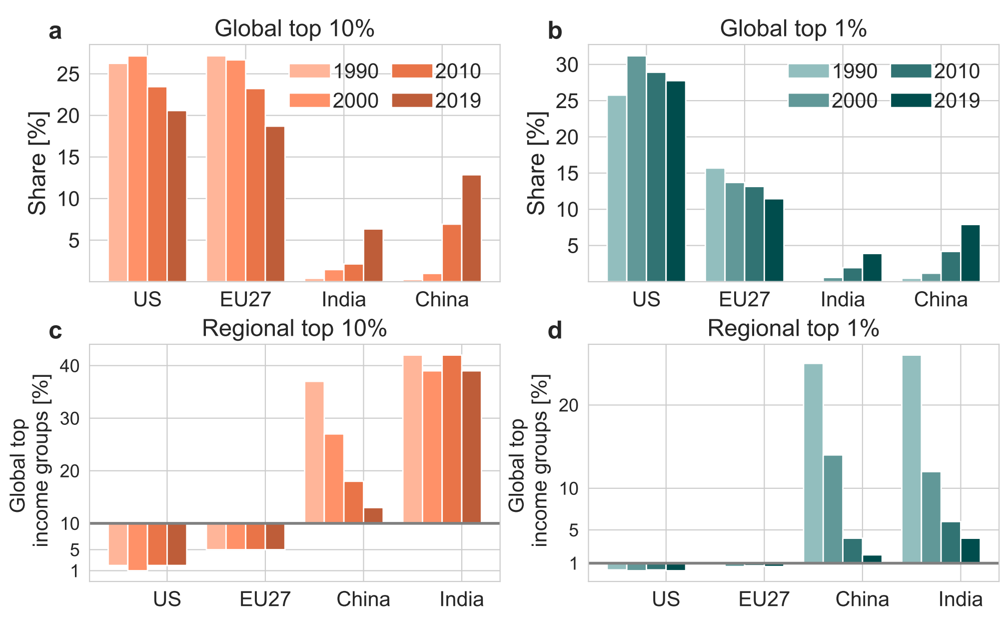

Supplementary Figure S1. |**Breakdown of global and region emitter groups. a-b,** Regional breakdown of the global top 10%/1%. **c-d,** Income thresholds of the regional top 10%/1% ranked against global income levels. Values below (above) bold grey line indicate regional top 10%/1% are wealthier (poorer) than global top 10%/1%. Data was taken from ref.[2] and processed for display.

Supplementary Table S1. |**Income thresholds for global income groups in 2019**. Yearly per capita income thresholds in 2019 [€] by income group. Data was taken from[2] and processed for display.

Group	Yearly per capita income threshold in 2019 [€]
top 80	2,450
top 60	5,330
top 40	11,330
top 20	24,640
top 10	42,980
top 5	67,540
top 1	147,200
top 0.1	537,770

Supplementary Table S2. |**Mean carbon emissions between 1990-2020 by region and emitter group.** First value indicates the mean relative contribution to global CO_2-e emissions by region and income group over 1990-2020. Second value indicates what the contribution would have been if every person contributed to global emissions equally. We then derive Climate Inequality Factors from group's actual contribution to emissions relative to their equal share. Values below (above) 1 indicate a group emits less (more) than their equal contribution. Data was taken from[1] and processed for display.

Region	Group	Actual contribution to global [%]	Equal contribution to global [%]	Relation
	all	100	-	-
	bottom 50	10.35	50	0.20
	middle 40	40.35	40	1
World	top 10	49.55	10	5
	top 1	16	1	16
	top 0.1	6.09	0.1	60
	all	19.54	4.49	4
	bottom 50	5.03	2.24	2
	middle 40	8.41	1.8	5
US	top 10	6.1	0.45	14
	top 1	1.93	0.04	43
	top 0.1	0.69	0	153
	all	13.96	6.16	2
	bottom 50	3.74	3.08	1
	middle 40	6.28	2.46	3
EU27	top 10	3.94	0.62	6
	top 1	1.05	0.06	17
	top 0.1	0.32	0.01	53
	all	4.59	17	0.3
	bottom 50	1.08	8.5	0.1
	middle 40	1.87	6.8	0.3
India	top 10	1.64	1.7	1
	top 1	0.51	0.17	3
	top 0.1	0.17	0.02	10
	all	16.43	20.6	0.8
	bottom 50	3.6	10.3	0.4
	middle 40	6.73	8.24	0.8
China	top 10	6.1	2.06	3
	top 1	2.03	0.21	10
	top 0.1	0.75	0.02	36

2 ATTRIBUTION OF GLOBAL MEAN TEMPERATURES AND SENSITIVITY TO EMISSION PROFILES

A detailed account of attributable GMT levels for all three disaggregation assumptions is given in Table S3. Additionally, Fig. S2 visually shows the sensitivity of attributable GMT levels to different compositions of GHGs. For each of the emitter groups, the same amount of CO_2-e emissions was removed in each year, only the disaggregation of these emissions into CH_4, N_2O and CO_2 was varied. Overall, the attribution results are highly sensitive to the composition of emissions. For example, 45% of the GMT increase since 1990 would be attributable to the top 10% if they only emitted carbon while 93% would be attributable if they emitted mainly CH_4 and N_2O. Therefore, if emissions were to consist primarily of CO_2, the inequality in contributions to GMT levels persists, but is slightly below the inequality in GHG basket emissions. For the non-CO_2-case, warming inequality is strongly amplified.

The high discrepancy in attributable results is related to the different global warming potentials (GWPs) of the the individual gases. For example, CH_4 has 27-30 times the GWP of CO_2 over a 100 year timescale while it has 80-83 times the GWP over a 20 year timescale[3]. This implies that effects of removing CH_4 are palpable on relatively short timescales already. Typically, GWPs over 100 years are used to convert CH_4 emissions into CO_2-e emissions. Doing so naturally causes discrepancies when observing the impacts of reduced CH_4 emissions over a 30 year time period as done in this study. The disaggregation into individual gases raises the question as to which timescale to use to convert GHGs into CO_2-e emissions and the overall gas mix. Better datasets that describe how the composition of individual emissions varies with incomes are needed to constrain our assumptions. The lacking availability of such datasets is currently limiting the accuracy of our study.

This sensitivity to GHG composition also highlights the enormous role CH_4 plays in reaching near-term temperature targets. Reducing CH_4 emissions is extremely effective in mitigating near-term global mean temperatures and in immediately reducing risks from climate extremes, while CO_2 reductions play out over longer timescales.

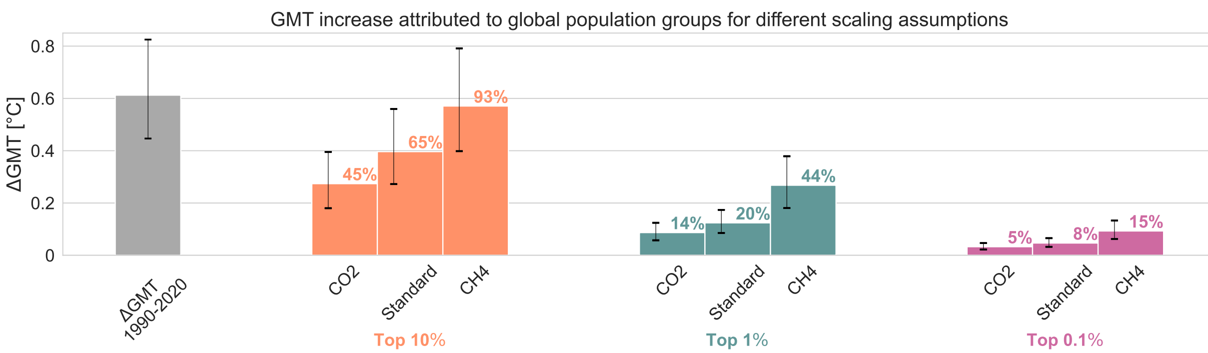

Supplementary Figure S2. | **GMT increase attributable to global emitter groups under different disaggregation assumptions**. Median GMT increase from 1990 to 2020 (grey bar), along with median GMT increase attributable to global top 10/1/0.1% (orange/teal/pink) for three different assumptions on how the basket emissions are decomposed into individual GHGs. We assume that basket emissions consist of only CO2, scale proportionally with the globally aggregated emissions (standard) and consist mainly of CH_4/N_2O. Percentage values above bars are relative to total GMT increase since 1990. Vertical lines correspond to 5^{th}-95^{th} uncertainty ranges. Estimates are computed from 600 ensemble members each.

Supplementary Table S3. |**Attributed GMT by emitter group.** Table includes GMT increase attributable to specific emitter groups. We display data for all three disaggregation assumptions (CO_2, Standard, non-CO_2) and provide the mean along with the 5th-95th uncertainty ranges (natural variability and uncertainty in the global temperature response to emission changes). For historic data as forcing, no scaling assumption is required. Equal shares are relative to historic GMT increase. All values are in centigrad [°C]

Region	Group	CO_2			Standard			non-CO_2			Equal
		mean	5^{th}	95^{th}	mean	5^{th}	95^{th}	mean	5^{th}	95^{th}	share
World	historic	nan	nan	nan	0.612	0.447	0.825	nan	nan	nan	nan
	top 10	0.274	0.18	0.395	0.396	0.272	0.56	0.571	0.398	0.792	0.061
World	top 1	0.087	0.057	0.124	0.124	0.085	0.174	0.268	0.181	0.379	0.006
	top 0.1	0.033	0.022	0.047	0.047	0.032	0.065	0.093	0.063	0.133	0.001
	all	nan	nan	nan	0.15	0.103	0.21	nan	nan	nan	0.027
	top 10	0.033	0.022	0.047	0.046	0.032	0.065	0.089	0.06	0.126	0.003
US	top 1	0.01	0.007	0.015	0.015	0.01	0.02	0.027	0.018	0.038	<0.001
	top 0.1	0.004	0.002	0.005	0.005	0.004	0.007	0.01	0.007	0.014	<0.00
	all	nan	nan	nan	0.106	0.072	0.147	nan	nan	nan	0.038
	top 10	0.021	0.014	0.03	0.029	0.02	0.041	0.055	0.037	0.077	0.004
EU27	top 1	0.006	0.004	0.008	0.008	0.005	0.011	0.014	0.01	0.02	<0.00
	top 0.1	0.002	0.001	0.002	0.002	0.002	0.003	0.004	0.003	0.006	<0.00
	all	nan	nan	nan	0.035	0.024	0.048	nan	nan	nan	0.104
	top 10	0.009	0.006	0.012	0.013	0.009	0.018	0.025	0.017	0.035	0.01
India	top 1	0.003	0.002	0.004	0.004	0.003	0.005	0.008	0.005	0.011	0.001
	top 0.1	0.001	0.001	0.001	0.001	0.001	0.002	0.003	0.002	0.004	<0.00
	all	nan	nan	nan	0.129	0.09	0.179	nan	nan	nan	0.126
	top 10	0.034	0.023	0.049	0.05	0.035	0.069	0.106	0.072	0.15	0.013
China	top 1	0.012	0.008	0.016	0.017	0.012	0.024	0.035	0.024	0.049	0.001
	top 0.1	0.004	0.003	0.006	0.006	0.004	0.009	0.013	0.009	0.018	<0.00

3 EARTH SYSTEM MODEL DATA

Emulator calibration. We configure our emulator on 24 individual Earth System Models (ESMs) from the Sixth Phase of the Coupled Model Intercomparison Project (CMIP6) (see Table S4) and rely on a single ensemble member for calibration (see ref.[4] for further details).

ESM data over India. For each ESM, we aggregate the training data from 1850-2020 over India (see Fig. S3). The total change in mean temperature trend is +0.67°C in July and +0.55°C in January. This is less than the modelled increase in GMT over the same period (+1.29°C). In addition, there is a large inter-model disagreement in the temperature estimates. We attribute both findings to the role air pollution effects play in India[5,6] and the difficulty in adequately modelling these effects. The CMIP6 ESMs were forced with controversial anthropogenic aerosol emissions leading to inconsistent patterns in aerosol optical depth that may lead to errors in regional trends over India and China[7]. As our emulator approximates individual ESMS and is calibrated on CMIP6 data, the emulator adopts this behaviour. In addition, we do not alter regional aerosol emissions, meaning these can plausibly mask regional emergence in trends of extreme events. All in all, this leads to comparably small attributable increases in heat and drought trends over India (and to a lesser extent over China).

Supplementary Table S4. | **Overview of the calibration ensemble used for generating emulations.** Table shows the 24 ESMs that are part of this study and the scenarios that are available for each model. The number of realisations includes only ensemble members that have data for all indicated scenarios. The training run column contains the identifier of the run that is used for training. See ref.[4] for more information on calibration.

Model name	Reference	Available scenarios	# of realisations	Training run
ACCESS-CM2	[8]	SSP1-2.6, SPP2-4.5, SPP3-7.0, SPP5-8.5	5	r1i1p1f1
ACCESS-ESM1-5	[9]	SSP1-2.6, SPP2-4.5, SPP3-7.0, SPP5-8.5	40	r1i1p1f1
AWI-CM-1-1-MR	[10]	SSP1-2.6, SPP2-4.5, SPP3-7.0, SPP5-8.5	1	r1i1p1f1
CESM2-WACCM	[11]	SSP1-2.6, SPP2-4.5, SPP3-7.0, SPP5-8.5	3	r1i1p1f1
CESM2	[12]	SSP1-2.6, SPP2-4.5, SPP3-7.0, SPP5-8.5	1	r1i1p1f1
CMCC-CM2-SR5	[13]	SSP1-2.6, SPP2-4.5, SPP3-7.0, SPP5-8.5	1	r1i1p1f1
CNRM-CM6-1-HR	[14]	SSP1-2.6, SPP2-4.5, SPP3-7.0, SPP5-8.5	1	r1i1p1f2
CNRM-CM6-1	[15]	SSP1-2.6, SPP2-4.5, SPP3-7.0, SPP5-8.5	6	r1i1p1f2
CNRM-ESM2-1	[16]	SSP1-1.9, SSP1-2.6, SPP2-4.5, SPP3-7.0, SPP5-8.5	5	r1i1p1f1
CanESM5	[17]	SSP1-1.9, SSP1-2.6, SPP2-4.5, SPP3-7.0, SPP5-8.5	50	r1i1p1f1
E3SM-1-1	[18]	SPP5-8.5	1	r1i1p1f1
FGOALS-f3-L	[19]	SSP1-2.6, SPP2-4.5, SPP3-7.0, SPP5-8.5	1	r1i1p1f1
FGOALS-g3	[20]	SSP1-1.9, SSP1-2.6, SPP2-4.5, SPP3-7.0, SPP5-8.5	4	r1i1p1f1
FIO-ESM-2-0	[21]	SSP1-2.6, SPP2-4.5, SPP3-7.0, SPP5-8.5	3	r1i1p1f1
HadGEM3-GC31-LL	[22]	SSP1-2.6, SPP2-4.5, SPP3-7.0, SPP5-8.5	4	r1i1p1f3
HadGEM3-GC31-MM	[23]	SSP1-2.6, SPP5-8.5	4	r1i1p1f3
IPSL-CM6A-LR	[24]	SSP1-1.9, SSP1-2.6, SPP2-4.5, SPP3-7.0, SPP5-8.5	7	r1i1p1f1
MPI-ESM1-2-HR	[25]	SSP1-2.6, SPP2-4.5, SPP3-7.0, SPP5-8.5	2	r1i1p1f1
MPI-ESM1-2-LR	[26]	SSP1-1.9, SSP1-2.6, SPP2-4.5, SPP3-7.0, SPP5-8.5	30	r1i1p1f1
MRI-ESM2-0	[27]	SSP1-1.9, SSP1-2.6, SPP2-4.5, SPP3-7.0, SPP5-8.5	6	r1i1p1f1
NESM3	[28]	SSP1-2.6, SPP2-4.5, SPP5-8.5	2	r1i1p1f1
NorESM2-LM	[29]	SSP1-2.6, SPP2-4.5, SPP3-7.0, SPP5-8.5	1	r1i1p1f1
NorESM2-MM	[30]	SSP1-2.6, SPP2-4.5, SPP3-7.0, SPP5-8.5	1	r1i1p1f1
UKESM1-0-LL	[31]	SSP1-2.6, SPP2-4.5, SPP3-7.0, SPP5-8.5	5	r1i1p1f2

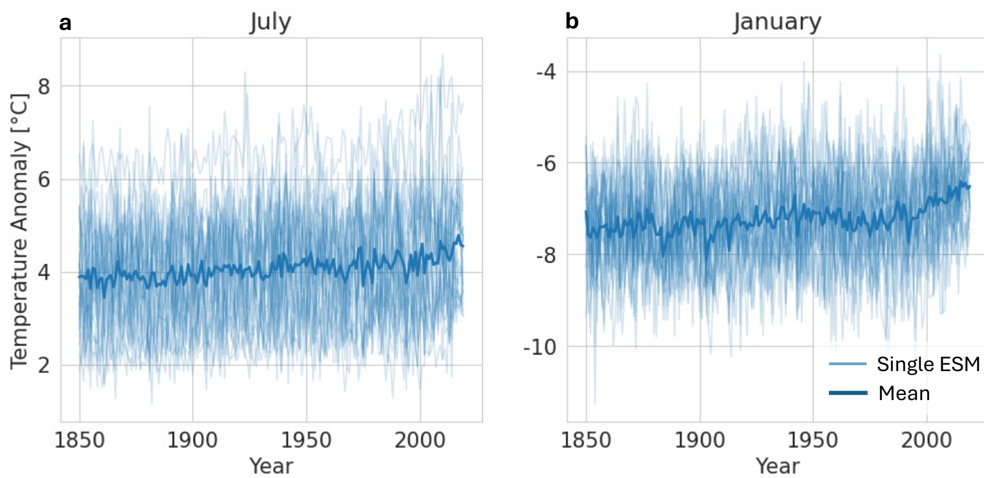

Supplementary Figure S3. | **ESM data over India**. Monthly mean temperature anomaly (relative to annual mean over reference period 1950-1900) in India for July (**a**) and for January (**b**). The timeseries were computed as an average over the training data for each ESM individually (24 thin lines). The mean over all models is highlighted as a bold line.

4 GRID-CELL LEVEL ATTRIBUTION RESULTS

In the main paper, we focus on results for frequency changes of extremes in the month with peak temperatures. Fig. S4 shows how the hottest month varies with grid-cell. In higher (lower) latitudes, i.e., above 30°N (30°S), this corresponds predominantly to the month of July (January). In the tropics, peak temperatures occur predominantly between March and June or between September and October. In Fig. S5 -S8 we show attributed frequency changes by month (January, April July and October). Additionally, we show results for attributed intensity changes in Fig. S10-S13.

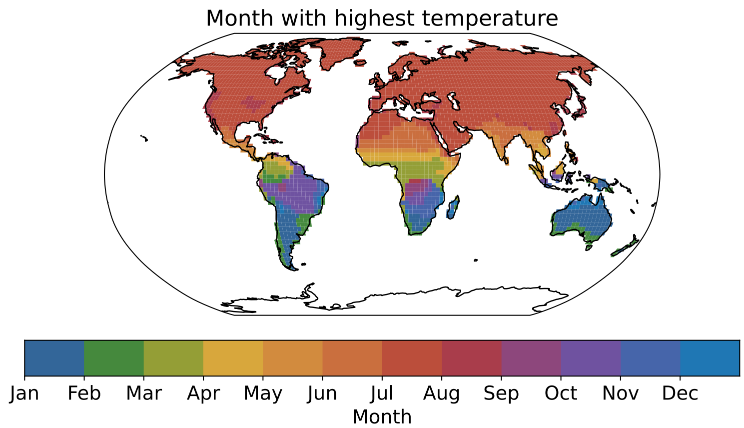

Supplementary Figure S4. | **Month with highest temperature by grid-cell**.

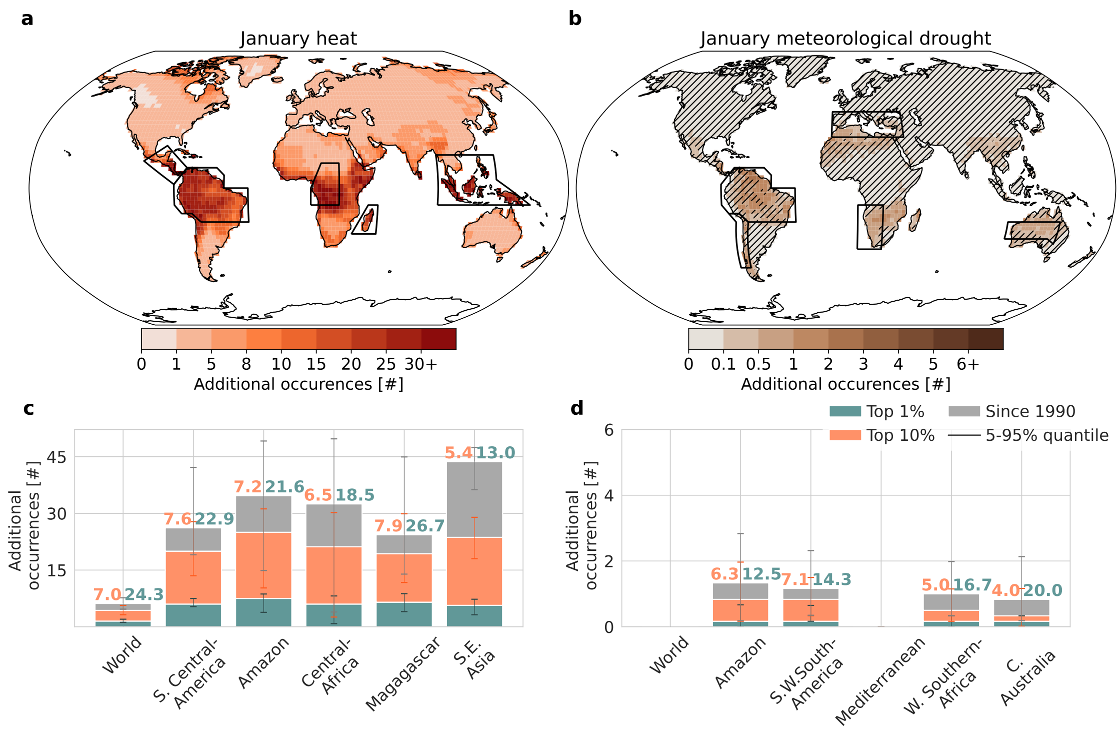

Supplementary Figure S5. | **Frequency change of 1-in-100 year monthly heat and meteorological drought events in January attributable to global top emitters. a-b,** Spatial distribution of the median number of heat (drought) extremes attributable to global top 10%. Median estimates are derived from 15,000 ensemble members. Hatched regions indicate insignificant results and/or insufficient model agreement. **c-d,** Median number of additional heat (drought) extremes by region (highlighted on map). Total increase in events between 1990 and 2020 (grey) and shares attributable to top 10% (1%) in orange (teal). Climate Inequality Factors indicating the group's contribution to extremes relative to the average contribution are given above the bars. Vertical lines correspond to 5th-95th uncertainty ranges. No data indicates insufficient agreement across a region. Distributions were derived by first computing median attribution results at each grid-cell (estimated from 15,000 ensemble members each) and then computing statistics across all grid-cells within each region.

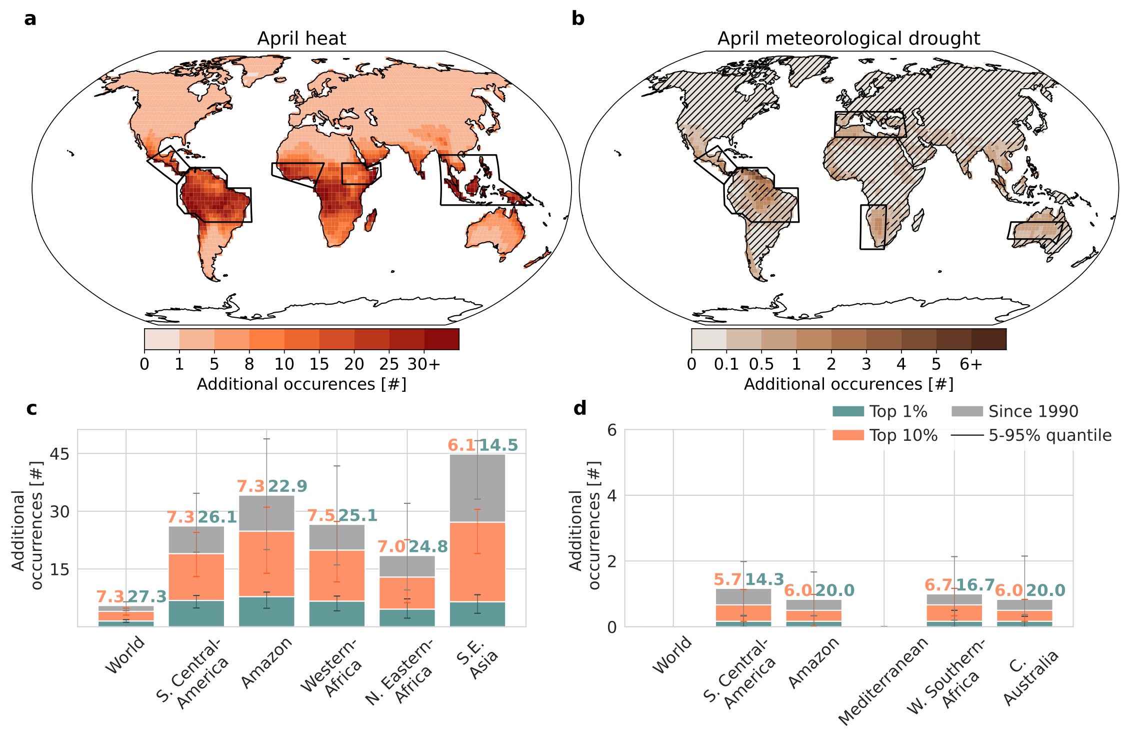

Supplementary Figure S6. | **Frequency change of 1-in-100 year monthly heat and meteorological drought events in April attributable to global top emitters. a-b,** Spatial distribution of the median number of heat (drought) extremes attributable to global top 10%. Median estimates are derived from 15,000 ensemble members. Hatched regions indicate insignificant results and/or insufficient model agreement. **c-d,** Median number of additional heat (drought) extremes by region (highlighted on map). Total increase in events between 1990 and 2020 (grey) and shares attributable to top 10% (1%) in orange (teal). Climate Inequality Factors indicating the group's contribution to extremes relative to the average contribution are given above the bars. Vertical lines correspond to 5^{th}-95^{th} uncertainty ranges. No data indicates insufficient agreement across a region. Distributions were derived by first computing median attribution results at each grid-cell (estimated from 15,000 ensemble members each) and then computing statistics across all grid-cells within each region.

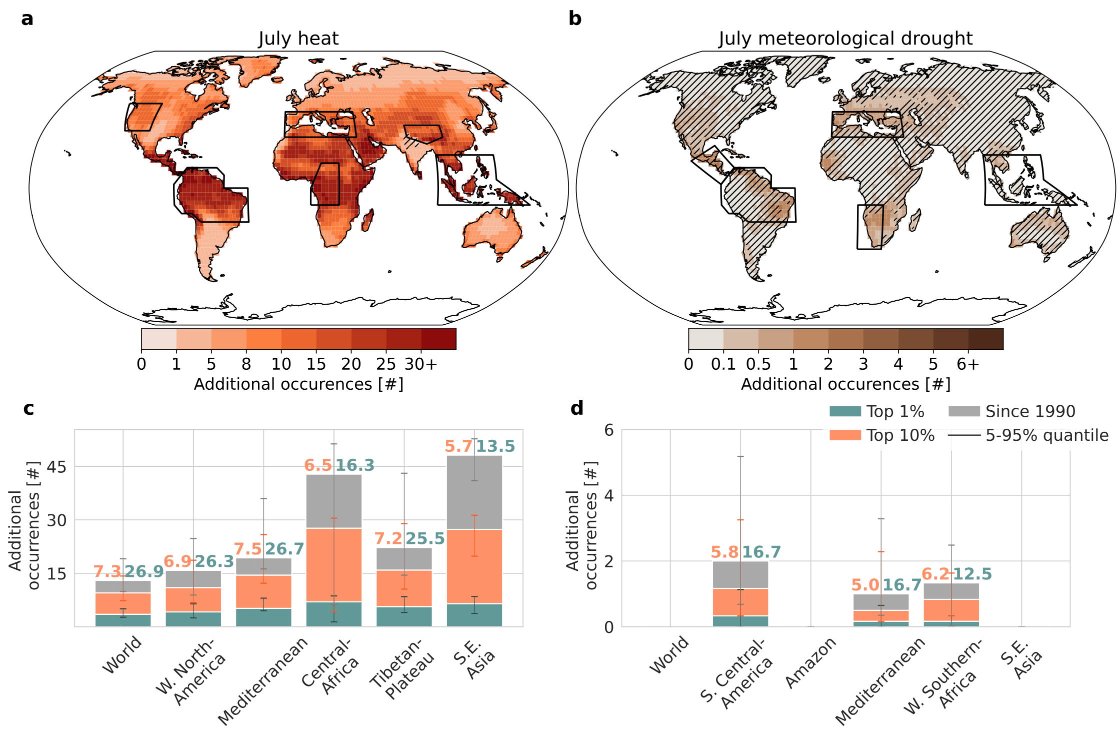

Supplementary Figure S7. | **Frequency change of 1-in-100 year monthly heat and meteorological drought events in July attributable to global top emitters. a-b,** Spatial distribution of the median number of heat (drought) extremes attributable to global top 10%. Median estimates are derived from 15,000 ensemble members. Hatched regions indicate insignificant results and/or insufficient model agreement. **c-d,** Median number of additional heat (drought) extremes by region (highlighted on map). Total increase in events between 1990 and 2020 (grey) and shares attributable to top 10% (1%) in orange (teal). Climate Inequality Factors indicating the group's contribution to extremes relative to the average contribution are given above the bars. Vertical lines correspond to 5th-95th uncertainty ranges. No data indicates insufficient agreement across a region. Distributions were derived by first computing median attribution results at each grid-cell (estimated from 15,000 ensemble members each) and then computing statistics across all grid-cells within each region.

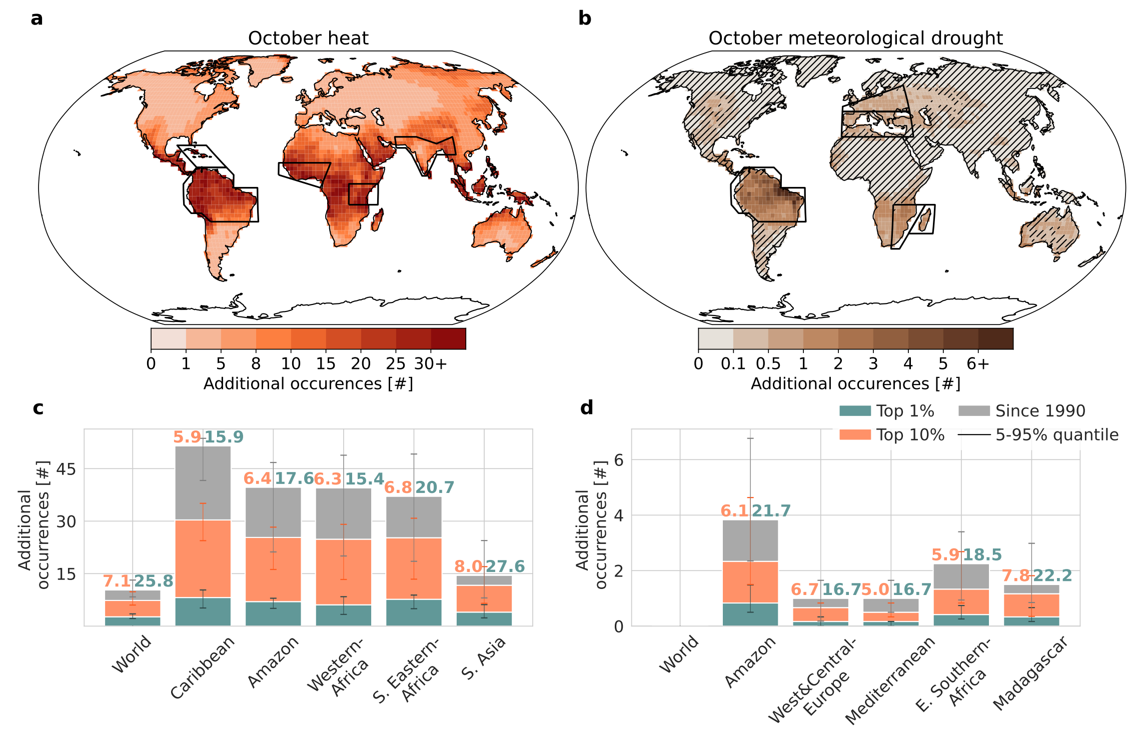

Supplementary Figure S8. | **Frequency change of 1-in-100 year monthly heat and meteorological drought events in October attributable to global top emitters. a-b,** Spatial distribution of the median number of heat (drought) extremes attributable to global top 10%. Median estimates are derived from 15,000 ensemble members. Hatched regions indicate insignificant results and/or insufficient model agreement. **c-d,** Median number of additional heat (drought) extremes by region (highlighted on map). Total increase in events between 1990 and 2020 (grey) and shares attributable to top 10% (1%) in orange (teal). Climate Inequality Factors indicating the group's contribution to extremes relative to the average contribution are given above the bars. Vertical lines correspond to 5th-95th uncertainty ranges. No data indicates insufficient agreement across a region. Distributions were derived by first computing median attribution results at each grid-cell (estimated from 15,000 ensemble members each) and then computing statistics across all grid-cells within each region.

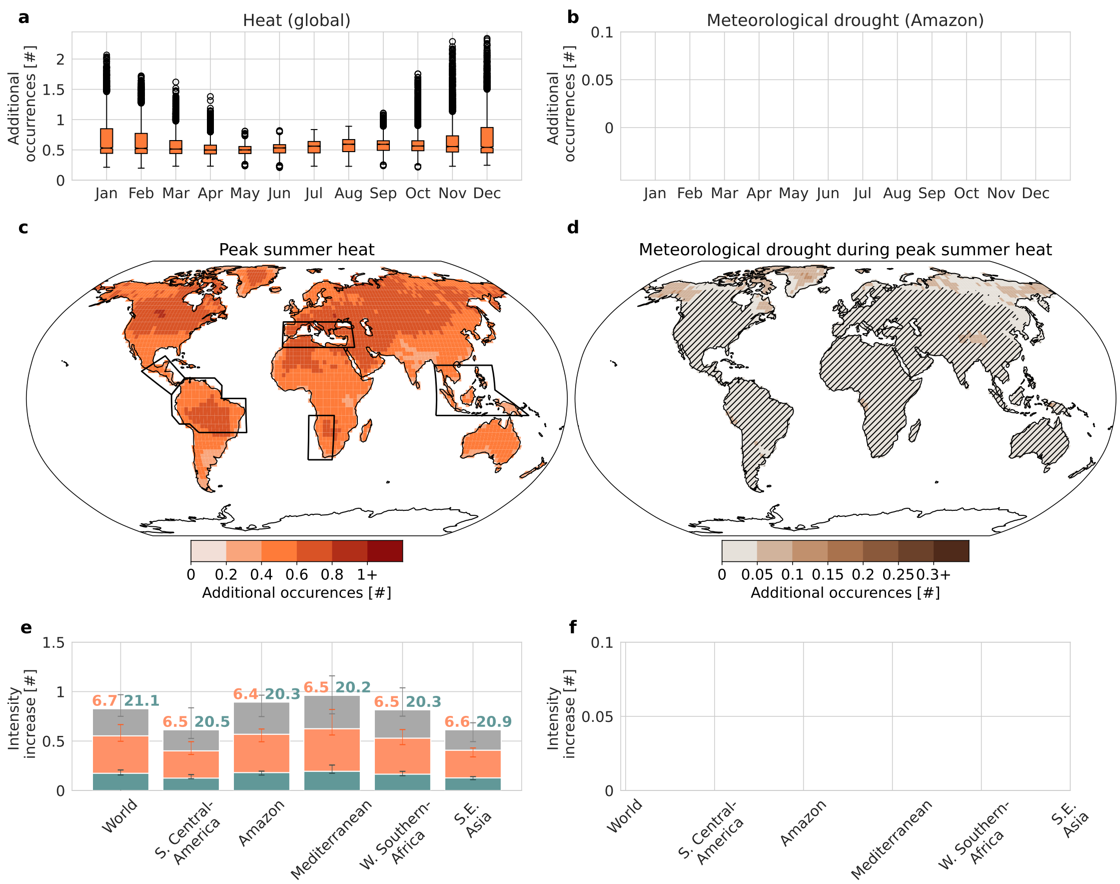

Supplementary Figure S9. | **Intensity change of 1-in-100 year monthly heat and meteorological drought extremes during months with peak summer heat attributable to global top emitters. a-b,** Spatial distribution of the median intensity increase of heat (drought) extremes attributable to global top 10%. Median estimates are derived from 15,000 ensemble members. Hatched regions indicate insignificant results and/or insufficient model agreement. **c-d,** Median intensity increase of heat (drought) extremes by region (highlighted on map). Total increase between 1990 and 2020 (grey) and shares attributable to top 10% (1%) in orange (teal). Climate Inequality Factors indicating the group's contribution to extremes relative to the average contribution are given above the bars. Vertical lines correspond to 5^{th}-95^{th} uncertainty ranges. No data indicates insufficient agreement across a region. Distributions were derived by first computing median attribution results at each grid-cell (estimated from 15,000 ensemble members each) and then computing statistics across all grid-cells within each region.

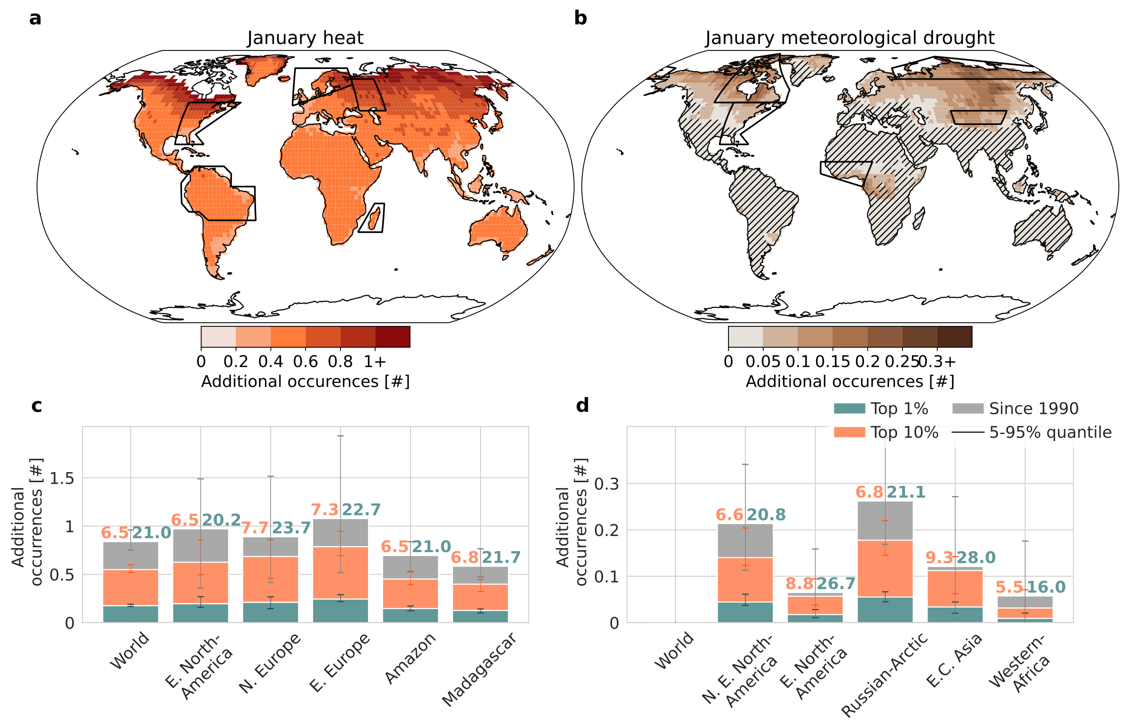

Supplementary Figure S10. | **Intensity change of 1-in-100 year monthly heat and meteorological drought extremes in January attributable to global top emitters. a-b,** Spatial distribution of the median intensity increase of heat (drought) extremes attributable to global top 10%. Median estimates are derived from 15,000 ensemble members. Hatched regions indicate insignificant results and/or insufficient model agreement. **c-d,** Median intensity increase of heat (drought) extremes by region (highlighted on map). Total increase between 1990 and 2020 (grey) and shares attributable to top 10% (1%) in orange (teal). Climate Inequality Factors indicating the group's contribution to extremes relative to the average contribution are given above the bars. Vertical lines correspond to 5^{th}-95^{th} uncertainty ranges. No data indicates insufficient agreement across a region. Distributions were derived by first computing median attribution results at each grid-cell (estimated from 15,000 ensemble members each) and then computing statistics across all grid-cells within each region.

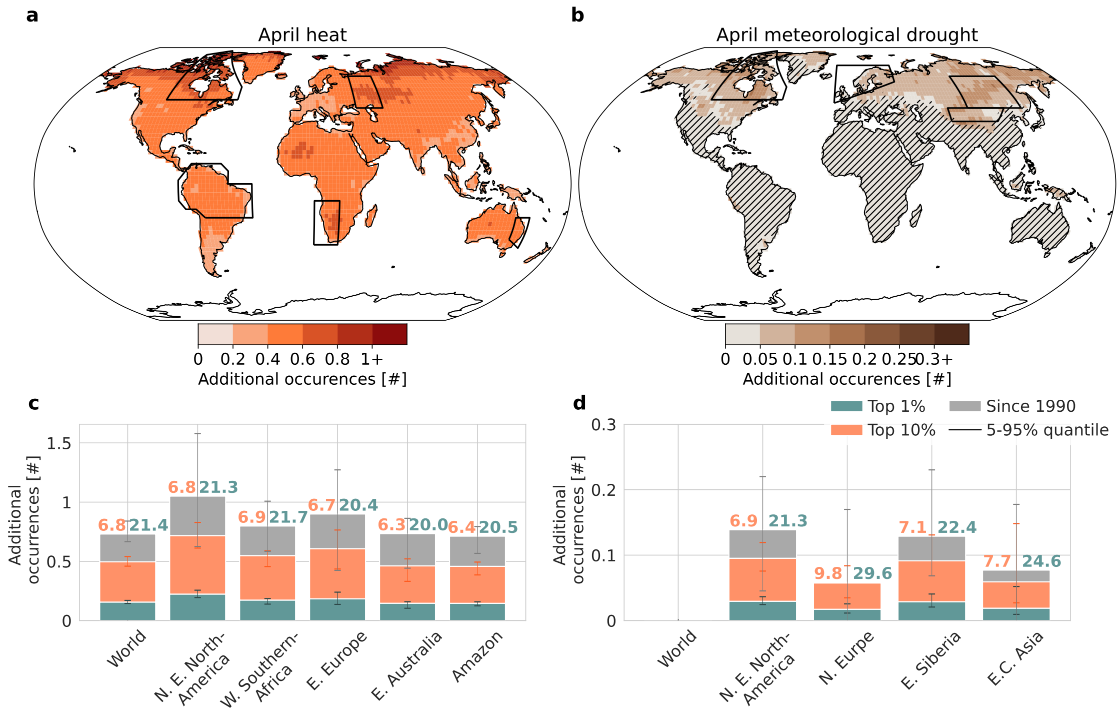

Supplementary Figure S11. | **Intensity change of 1-in-100 year monthly heat and meteorological drought extremes in April attributable to global top emitters. a-b,** Spatial distribution of the median intensity increase of heat (drought) extremes attributable to global top 10%. Median estimates are derived from 15,000 ensemble members. Hatched regions indicate insignificant results and/or insufficient model agreement. **c-d,** Median intensity increase of heat (drought) extremes by region (highlighted on map). Total increase between 1990 and 2020 (grey) and shares attributable to top 10% (1%) in orange (teal). Climate Inequality Factors indicating the group's contribution to extremes relative to the average contribution are given above the bars. Vertical lines correspond to 5th-95th uncertainty ranges. No data indicates insufficient agreement across a region. Distributions were derived by first computing median attribution results at each grid-cell (estimated from 15,000 ensemble members each) and then computing statistics across all grid-cells within each region.

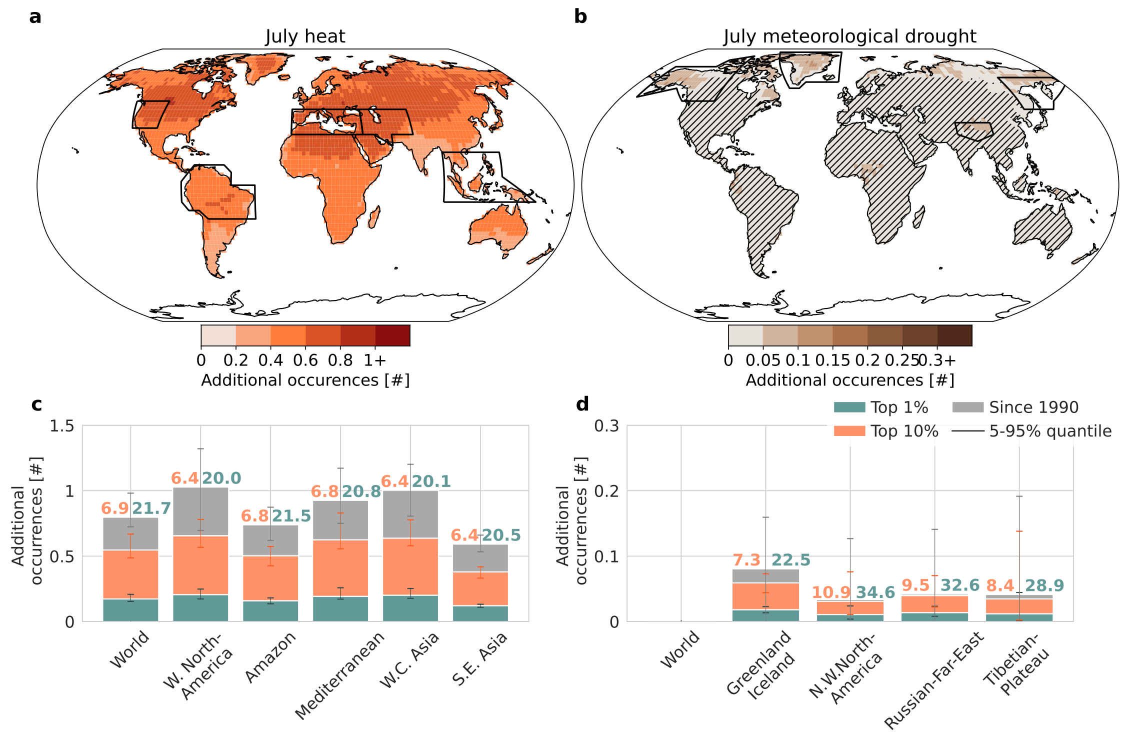

Supplementary Figure S12. | **Intensity change of 1-in-100 year monthly heat and meteorological drought extremes in July attributable to global top emitters. a-b,** Spatial distribution of the median intensity increase of heat (drought) extremes attributable to global top 10%. Median estimates are derived from 15,000 ensemble members. Hatched regions indicate insignificant results and/or insufficient model agreement. **c-d,** Median intensity increase of heat (drought) extremes by region (highlighted on map). Total increase between 1990 and 2020 (grey) and shares attributable to top 10% (1%) in orange (teal). Climate Inequality Factors indicating the group's contribution to extremes relative to the average contribution are given above the bars. Vertical lines correspond to 5^{th}-95^{th} uncertainty ranges. No data indicates insufficient agreement across a region. Distributions were derived by first computing median attribution results at each grid-cell (estimated from 15,000 ensemble members each) and then computing statistics across all grid-cells within each region.

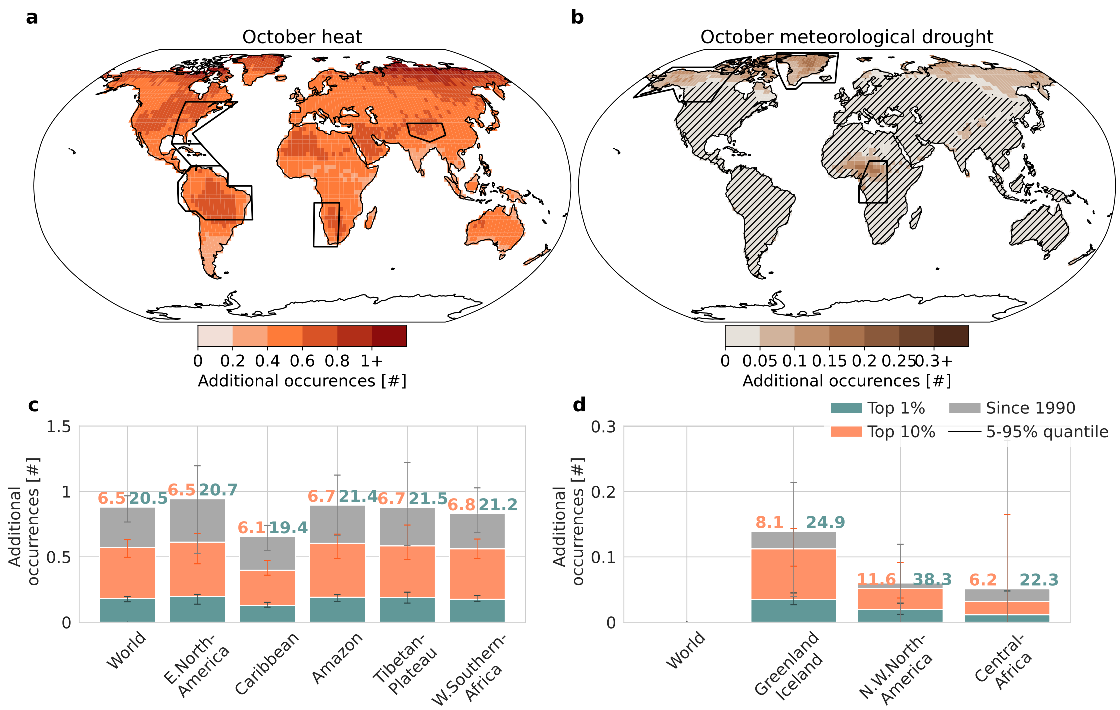

Supplementary Figure S13. | **Intensity change of 1-in-100 year monthly heat and meteorological drought extremes in October attributable to global top emitters. a-b,** Spatial distribution of the median intensity increase of heat (drought) extremes attributable to global top 10%. Median estimates are derived from 15,000 ensemble members. Hatched regions indicate insignificant results and/or insufficient model agreement. **c-d,** Median intensity increase of heat (drought) extremes by region (highlighted on map). Total increase between 1990 and 2020 (grey) and shares attributable to top 10% (1%) in orange (teal). Climate Inequality Factors indicating the group's contribution to extremes relative to the average contribution are given above the bars. Vertical lines correspond to 5^{th}-95^{th} uncertainty ranges. No data indicates insufficient agreement across a region. Distributions were derived by first computing median attribution results at each grid-cell (estimated from 15,000 ensemble members each) and then computing statistics across all grid-cells within each region.

5 RESULTS FOR DIFFERENT DROUGHT INDICATORS

We conduct our attribution analysis using two different drought indicators. In the main of the paper, we focus on the Standardized Precipitation Index computed over a 3 month period (SPI-3) as recommended to monitor meteorological droughts[32]. Here, we show results for results relying on the Standardized Evapotranspiration Index computed over a 3 month period (SPEI-3) via the Thornthwaite method[33]. The two indicators differ as SPEI takes changes in water demand into account by including potential evapotranspiration (PET) during the computation of wet and dry spells. Given restrictions in data availability we compute PET demands solely from temperature data following the Thornthwaite equation. This introduces a bias in the PET estimates towards a steady increase with increasing temperatures, which neglects the influence of changing wind speeds, relative humidity and solar radiation amounts[32,34], leading to an overestimation of the warming-driven drying trend. We include the SPEI indicator as an upper bound for attributable results and note that true drought risks fall between estimates from SPI-3 (see Fig. **??** and Fig. S5-S8) and the estimates from SPEI-3 shown in Fig. S14-S17). The two indicators agree in the direction of attributable drought risks over the Amazon, Central America, the Mediterranean, Australia and Southern Africa. However, results from SPEI are about 10 times higher which reflects the impacts of temperature in the drought projections. The SPEI-3 strongly deviates from SPI-3 estimates over deserts (e.g., Sahara desert or Arabian peninsula desert). Results from both indicators in deserts should be taken with caution given precipitation is extremely low over deserts, meaning even small precipitation amounts may have a strong impact on drought projections.

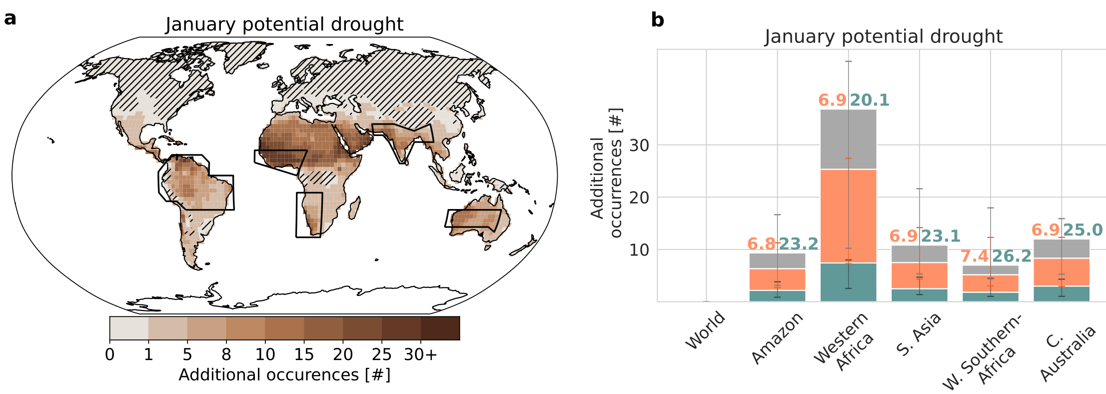

Supplementary Figure S14. | **Frequency change of 1-in-100 year potential drought events in January attributable to global top emitters. a,** Spatial distribution of the median number of drought extremes attributable to global top 10%. Median estimates are derived from 15,000 ensemble members. Hatched regions indicate insignificant results and/or insufficient model agreement. **b,** Median number of additional drought extremes by region (highlighted on map). Total increase in events between 1990 and 2020 (grey) and shares attributable to top 10% (1%) in orange (teal). Climate Inequality Factors indicating the group's contribution to extremes relative to the average contribution are given above the bars. Vertical lines correspond to 5^{th}-95^{th} uncertainty ranges. No data indicates insufficient agreement across a region. Distributions were derived by first computing median attribution results at each grid-cell (estimated from 15,000 ensemble members each) and then computing statistics across all grid-cells within each region.

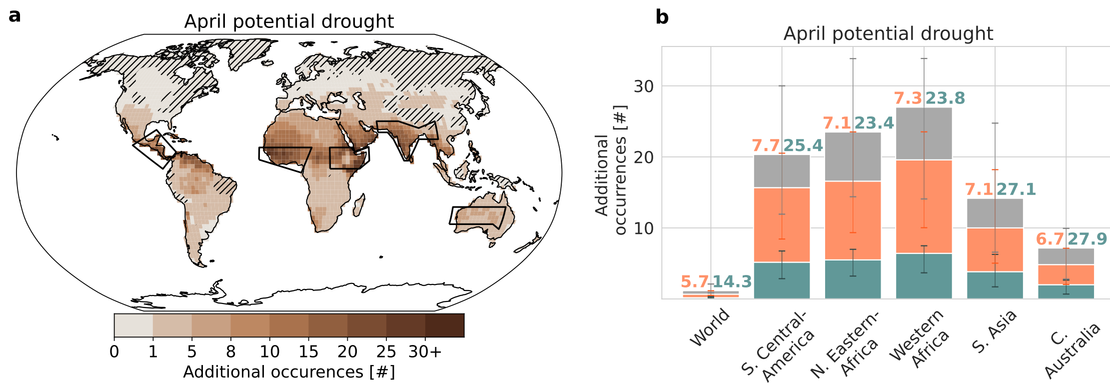

Supplementary Figure S15. | **Frequency change of 1-in-100 year potential drought events in April attributable to global top emitters. a,** Spatial distribution of the median number of drought extremes attributable to global top 10%. Median estimates are derived from 15,000 ensemble members. Hatched regions indicate insignificant results and/or insufficient model agreement. **b,** Median number of additional drought extremes by region (highlighted on map). Total increase in events between 1990 and 2020 (grey) and shares attributable to top 10% (1%) in orange (teal). Climate Inequality Factors indicating the group's contribution to extremes relative to the average contribution are given above the bars. Vertical lines correspond to 5^{th}-95^{th} uncertainty ranges. No data indicates insufficient agreement across a region. Distributions were derived by first computing median attribution results at each grid-cell (estimated from 15,000 ensemble members each) and then computing statistics across all grid-cells within each region.

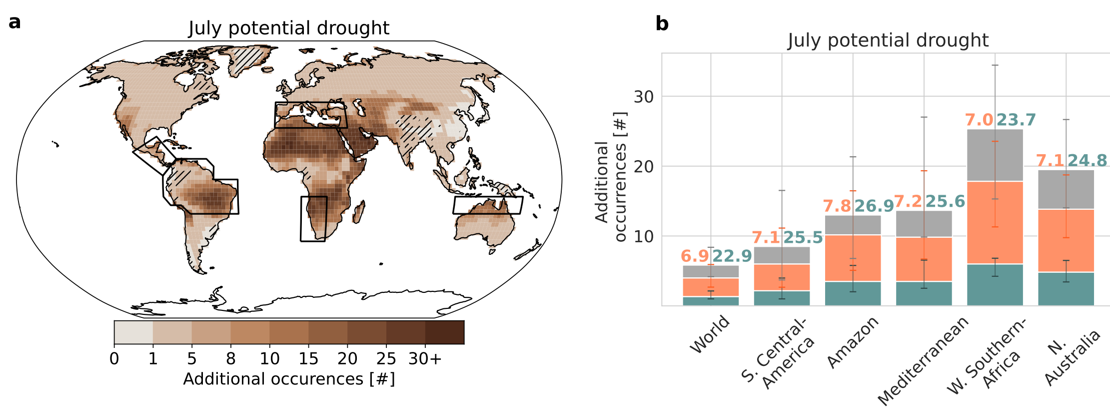

Supplementary Figure S16. | **Frequency change of 1-in-100 year potential drought events in July attributable to global top emitters. a,** Spatial distribution of the median number of drought extremes attributable to global top 10%. Median estimates are derived from 15,000 ensemble members. Hatched regions indicate insignificant results and/or insufficient model agreement. **b,** Median number of additional drought extremes by region (highlighted on map). Total increase in events between 1990 and 2020 (grey) and shares attributable to top 10% (1%) in orange (teal). Climate Inequality Factors indicating the group's contribution to extremes relative to the average contribution are given above the bars. Vertical lines correspond to 5^{th}-95^{th} uncertainty ranges. No data indicates insufficient agreement across a region. Distributions were derived by first computing median attribution results at each grid-cell (estimated from 15,000 ensemble members each) and then computing statistics across all grid-cells within each region.

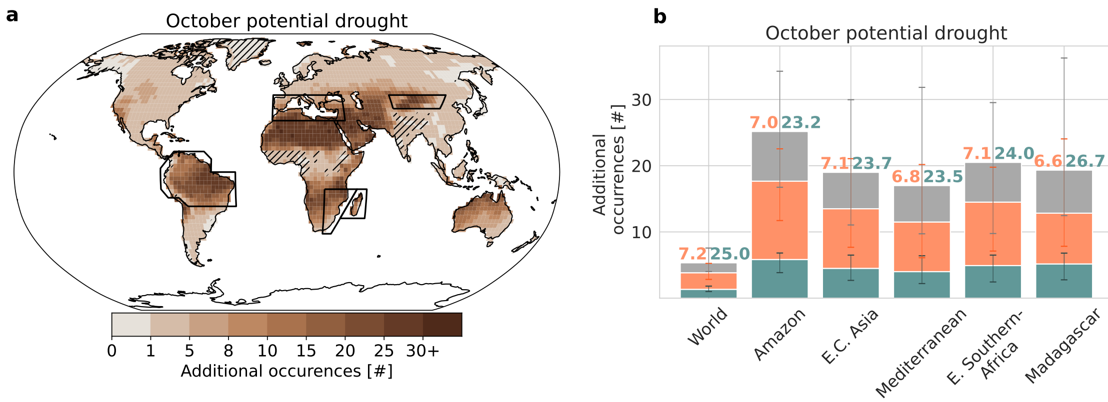

Supplementary Figure S17. | **Frequency change of 1-in-100 year potential drought events in October attributable to global top emitters. a,** Spatial distribution of the median number of drought extremes attributable to global top 10%. Median estimates are derived from 15,000 ensemble members. Hatched regions indicate insignificant results and/or insufficient model agreement. **b,** Median number of additional drought extremes by region (highlighted on map). Total increase in events between 1990 and 2020 (grey) and shares attributable to top 10% (1%) in orange (teal). Climate Inequality Factors indicating the group's contribution to extremes relative to the average contribution are given above the bars. Vertical lines correspond to 5th-95th uncertainty ranges. No data indicates insufficient agreement across a region. Distributions were derived by first computing median attribution results at each grid-cell (estimated from 15,000 ensemble members each) and then computing statistics across all grid-cells within each region.

6 RESULTS FOR DIFFERENT EVENT DEFINITIONS

In Fig. S18-S21, we explore the effect of different event definitions on attributable results. We find that the rarer the extreme the higher is the relative increase in probability ratio with increasing temperatures. We also find that with increasing rarity, the spatial disparity in attributable results increases.

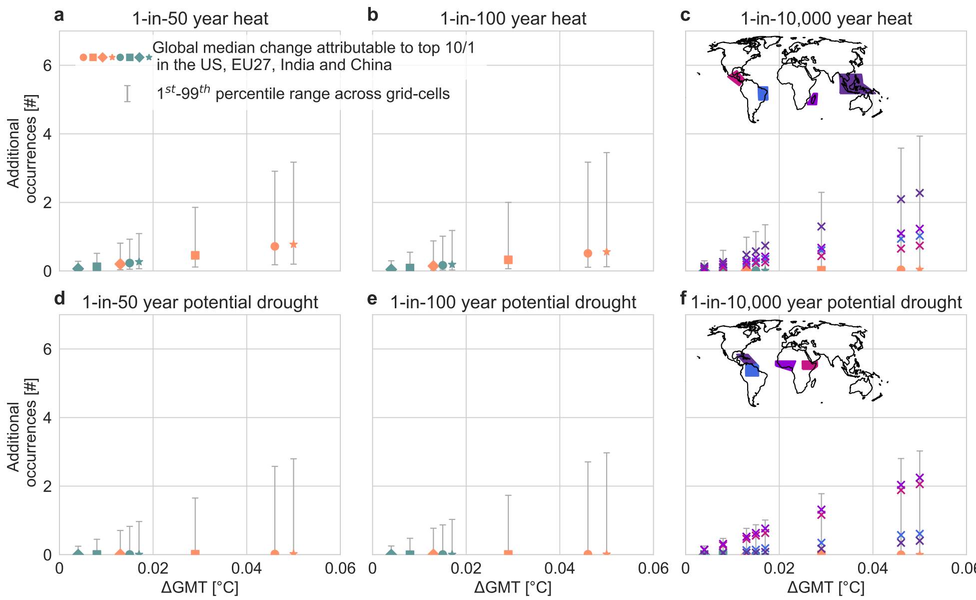

Supplementary Figure S18. | **Attributable extreme events for different event definitions in February. a-c,** Attributable 1-in-50/100/10,000 year heat events plotted against median attributed GMT increase. Orange (teal) symbols indicate attributable global median change for the emissions associated with the wealthiest 10% (1%) in the US (circle), EU27 (square), India (diamond) and China (star). Whiskers indicate distribution across grid-cells (1^{st}-99^{th} percentile range). **a-f,** Same as a-c but for potential drought events. All distributions were derived by first computing median attributable results by grid-cell (from 15,000 ensemble members) and then computing statistics across all 2652 grid-cells.

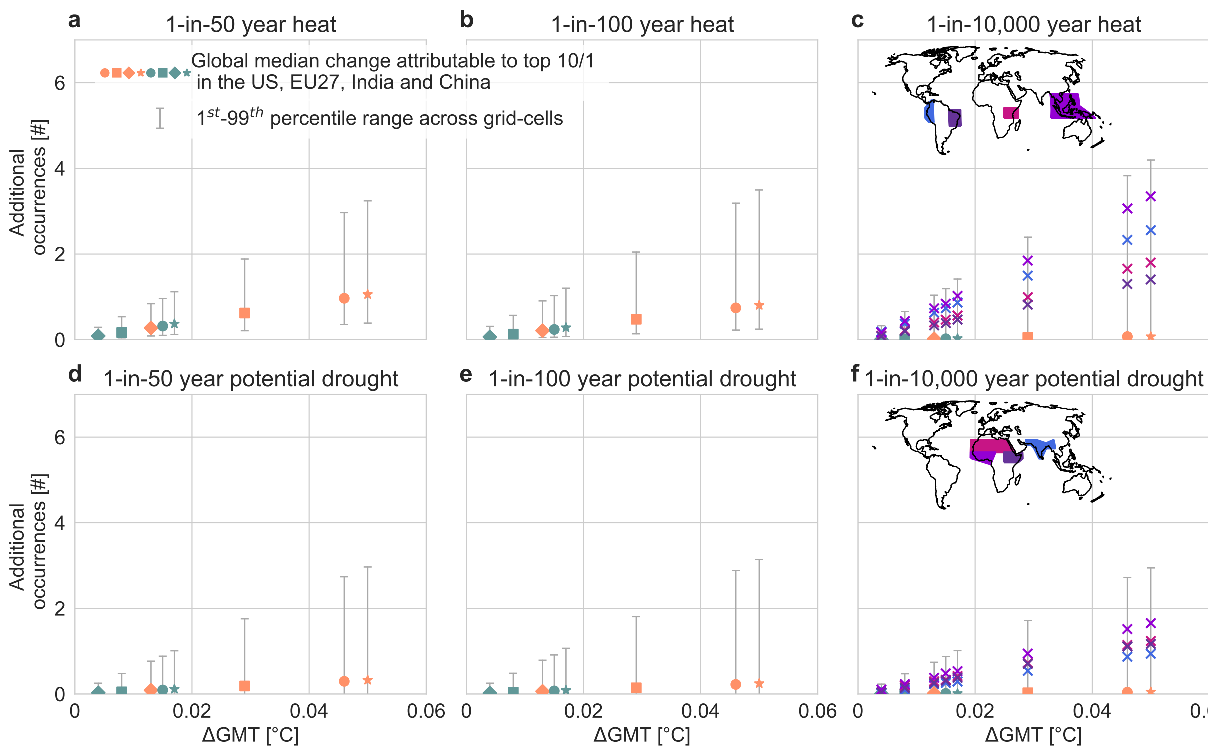

Supplementary Figure S19. | **Attributable extreme events for different event definitions in May. a-c,** Attributable 1-in-50/100/10,000 year heat events plotted against median attributed GMT increase. Orange (teal) symbols indicate attributable global median change for the emissions associated with the wealthiest 10% (1%) in the US (circle), EU27 (square), India (diamond) and China (star). Whiskers indicate distribution across grid-cells (1^{st}-99^{th} percentile range). **a-f,** Same as a-c but for potential drought events. All distributions were derived by first computing median attributable results by grid-cell (from 15,000 ensemble members) and then computing statistics across all 2652 grid-cells.

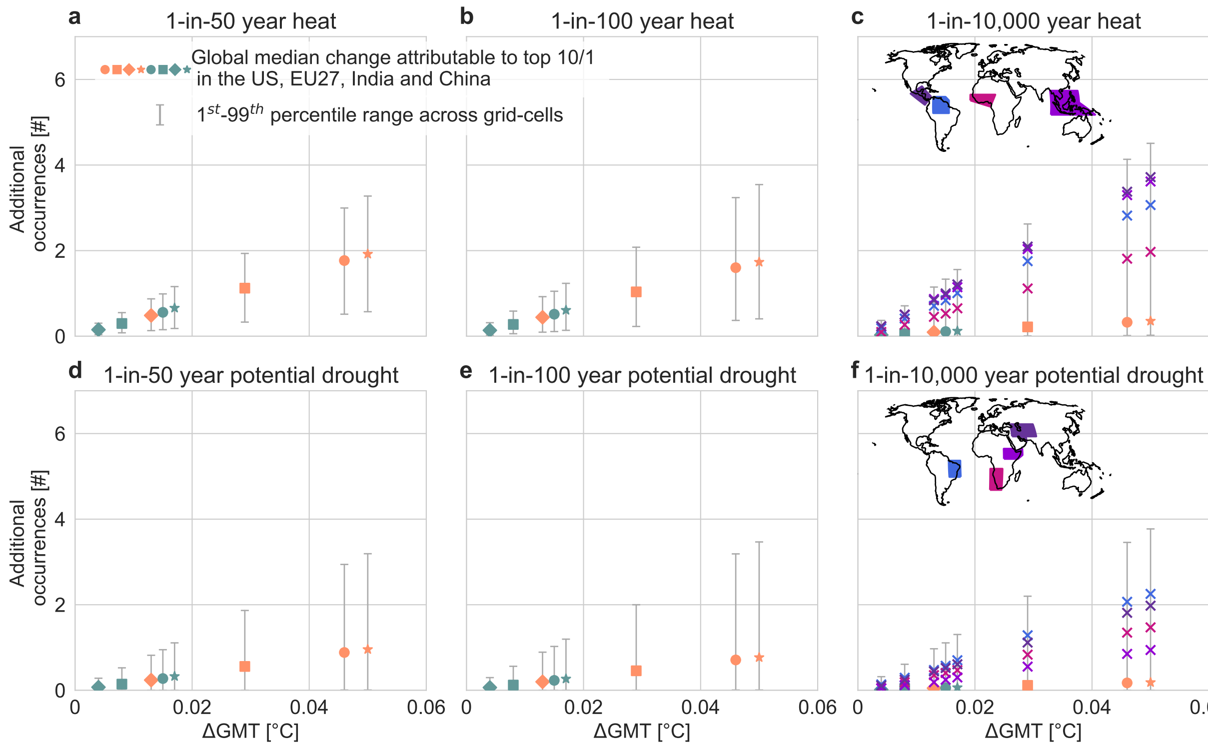

Supplementary Figure S20. | **Attributable extreme events for different event definitions in August. a-c,** Attributable 1-in-50/100/10,000 year heat events plotted against median attributed GMT increase. Orange (teal) symbols indicate attributable global median change for the emissions associated with the wealthiest 10% (1%) in the US (circle), EU27 (square), India (diamond) and China (star). Whiskers indicate distribution across grid-cells (1^{st}-99^{th} percentile range). **a-f,** Same as a-c but for potential drought events. All distributions were derived by first computing median attributable results by grid-cell (from 15,000 ensemble members) and then computing statistics across all 2652 grid-cells.

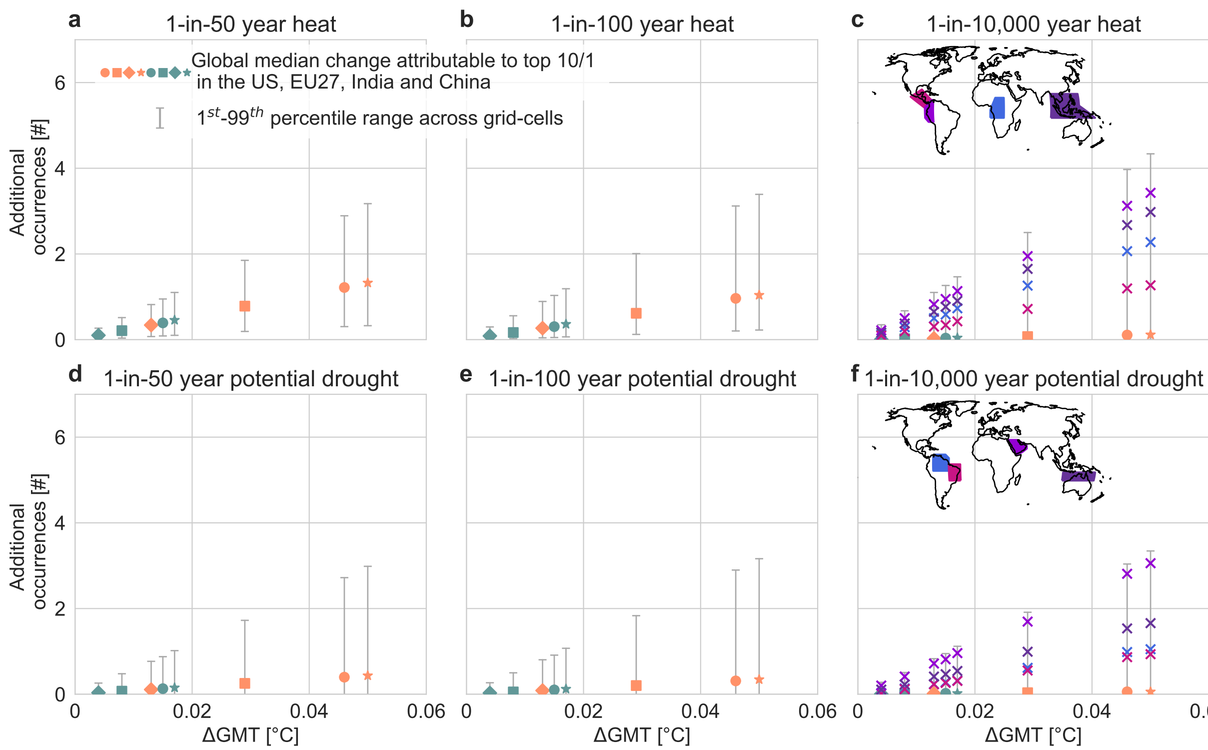

Supplementary Figure S21. | **Attributable extreme events for different event definitions in November. a-c,** Attributable 1-in-50/100/10,000 year heat events plotted against median attributed GMT increase. Orange (teal) symbols indicate attributable global median change for the emissions associated with the wealthiest 10% (1%) in the US (circle), EU27 (square), India (diamond) and China (star). Whiskers indicate distribution across grid-cells (1^{st}-99^{th} percentile range). **a-f,** Same as a-c but for potential drought events. All distributions were derived by first computing median attributable results by grid-cell (from 15,000 ensemble members) and then computing statistics across all 2652 grid-cells.

REFERENCES

1. Chancel, L. Global carbon inequality over 1990–2019. *Nature Sustainability* **5,** 931–938. https://doi.org/10.1038/s41893-022-00955-z (2022).
2. World Inequality Database. *WID.world: The World Inequality Database* Accessed: 2024-11-01. n.d. https://wid.world/.
3. Masson-Delmotte, V. *et al. IPCC, 2021: Summary for policymakers. in: Climate change 2021: The physical science basis. contribution of working group i to the sixth assessment report of the intergovernmental panel on climate change* 2021.
4. Schöngart, S. *et al.* Introducing the MESMER-M-TPv0.1.0 module: Spatially Explicit Earth System Model Emulation for Monthly Precipitation and Temperature. *EGUsphere* **2024,** 1–51. https://egusphere.copernicus.org/preprints/2024/egusphere-2024-278/ (2024).
5. Cohen, S. & Stanhill, G. in *Climate Change (Second Edition)* (ed Letcher, T. M.) Second Edition, 491–511 (Elsevier, Boston, 2016). ISBN: 978-0-444-63524-2. https://www.sciencedirect.com/science/article/pii/B9780444635242000294.
6. Jia, A., Liang, S., Wang, D., Jiang, B. & Zhang, X. Air pollution slows down surface warming over the Tibetan Plateau. *Atmospheric Chemistry and Physics* **20,** 881–899 (2020).
7. Wang, Z. *et al.* Incorrect Asian aerosols affecting the attribution and projection of regional climate change in CMIP6 models. *npj Climate and Atmospheric Science* **4,** 2 (2021).
8. Dix, M. *et al. CSIRO-ARCCSS ACCESS-CM2 model output prepared for CMIP6 ScenarioMIP* 2019. https://doi.org/10.22033/ESGF/CMIP6.2285.
9. Ziehn, T. *et al. CSIRO ACCESS-ESM1.5 model output prepared for CMIP6 ScenarioMIP* 2019. https://doi.org/10.22033/ESGF/CMIP6.2291.
10. Semmler, T. *et al. AWI AWI-CM1.1MR model output prepared for CMIP6 ScenarioMIP* 2019. https://doi.org/10.22033/ESGF/CMIP6.376.
11. Danabasoglu, G. *NCAR CESM2-WACCM model output prepared for CMIP6 ScenarioMIP* 2019. https://doi.org/10.22033/ESGF/CMIP6.10026.
12. Danabasoglu, G. *NCAR CESM2 model output prepared for CMIP6 ScenarioMIP* 2019. https://doi.org/10.22033/ESGF/CMIP6.2201.
13. Lovato, T. & Peano, D. *CMCC CMCC-CM2-SR5 model output prepared for CMIP6 ScenarioMIP* 2020. https://doi.org/10.22033/ESGF/CMIP6.1365.
14. Voldoire, A. *CNRM-CERFACS CNRM-CM6-1-HR model output prepared for CMIP6 ScenarioMIP* 2019. https://doi.org/10.22033/ESGF/CMIP6.1388.
15. Voldoire, A. *CNRM-CERFACS CNRM-CM6-1 model output prepared for CMIP6 ScenarioMIP* 2019. https://doi.org/10.22033/ESGF/CMIP6.1384.
16. Seferian, R. *CNRM-CERFACS CNRM-ESM2-1 model output prepared for CMIP6 ScenarioMIP* 2019. https://doi.org/10.22033/ESGF/CMIP6.1395.
17. Swart, N. C. *et al. CCCma CanESM5 model output prepared for CMIP6 ScenarioMIP* 2019. https://doi.org/10.22033/ESGF/CMIP6.1317.
18. Bader, D. C., Leung, R., Taylor, M. & McCoy, R. B. *E3SM-Project E3SM1.1 model output prepared for CMIP6 ScenarioMIP* 2020. https://doi.org/10.22033/ESGF/CMIP6.15103.
19. YU, Y. *CAS FGOALS-f3-L model output prepared for CMIP6 ScenarioMIP* 2019. https://doi.org/10.22033/ESGF/CMIP6.2046.
20. Li, L. *CAS FGOALS-g3 model output prepared for CMIP6 ScenarioMIP* 2019. https://doi.org/10.22033/ESGF/CMIP6.2056.
21. Song, Z. *et al. FIO-QLNM FIO-ESM2.0 model output prepared for CMIP6 ScenarioMIP* 2019. https://doi.org/10.22033/ESGF/CMIP6.9051.

22. Good, P. *MOHC HadGEM3-GC31-LL model output prepared for CMIP6 ScenarioMIP* 2019. https://doi.org/10.22033/ESGF/CMIP6.10845.

23. Jackson, L. *MOHC HadGEM3-GC31-MM model output prepared for CMIP6 ScenarioMIP* 2020. https://doi.org/10.22033/ESGF/CMIP6.10846.

24. Boucher, O. *et al. IPSL IPSL-CM6A-LR model output prepared for CMIP6 ScenarioMIP* 2019. https://doi.org/10.22033/ESGF/CMIP6.1532.

25. Schupfner, M. *et al. DKRZ MPI-ESM1.2-HR model output prepared for CMIP6 ScenarioMIP* 2019. https://doi.org/10.22033/ESGF/CMIP6.2450.

26. Schupfner, M. *et al. DKRZ MPI-ESM1.2-LR model output prepared for CMIP6 ScenarioMIP* 2021. https://doi.org/10.22033/ESGF/CMIP6.15349.

27. Yukimoto, S. *et al. MRI MRI-ESM2.0 model output prepared for CMIP6 ScenarioMIP* 2019. https://doi.org/10.22033/ESGF/CMIP6.638.

28. Cao, J. *NUIST NESMv3 model output prepared for CMIP6 ScenarioMIP* 2019. https://doi.org/10.22033/ESGF/CMIP6.2027.

29. Seland, Ø. *et al. NCC NorESM2-LM model output prepared for CMIP6 ScenarioMIP* 2019. https://doi.org/10.22033/ESGF/CMIP6.604.

30. Bentsen, M. *et al. NCC NorESM2-MM model output prepared for CMIP6 ScenarioMIP* 2019. https://doi.org/10.22033/ESGF/CMIP6.608.

31. Good, P. *et al. MOHC UKESM1.0-LL model output prepared for CMIP6 ScenarioMIP* 2019. https://doi.org/10.22033/ESGF/CMIP6.1567.

32. Seneviratne, S. *et al.* Chapter 11: weather and climate extreme events in a changing climate. 2021 (2021).

33. Santos, C. N. *et al.* Monthly potential evapotranspiration estimated using the Thornthwaite method with gridded climate datasets in Southeastern Brazil. *Theoretical and Applied Climatology,* 1–18 (2024).

34. Sheffield, J., Wood, E. F. & Roderick, M. L. Little change in global drought over the past 60 years. *Nature* **491,** 435–438 (2012).